CHEMISTRY OF MATERIALS

pubs.acs.org/cm Article

Symmetry-Breaking Plasmonic Mesoporous Gold Nanoparticles with Large Pores

Asep Sugih Nugraha, Olga Guselnikova, Joel Henzie,* Jongbeom Na, Md Shahriar A. Hossain, Ömer Dag, Alan E. Rowan, and Yusuke Yamauchi*

Cite This: *Chem. Mater.* 2022, 34, 7256–7270 Read Online

ACCESS | Metrics & More | Article Recommendations | Supporting Information

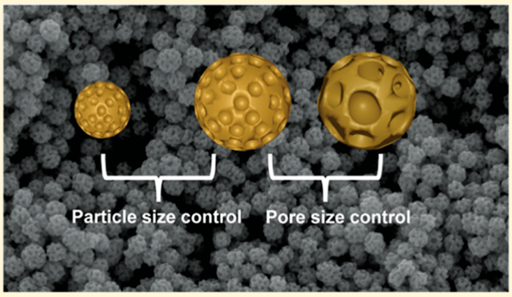

ABSTRACT: Creating free-standing gold nanoparticles (Au NPs) with large pores is desirable because the exterior and interior voids can enhance electrocatalytic activity, mass transport, and optical extinction properties. However, the high mobility and significant positive reduction potential of Au precursors make it challenging to create Au NPs with pores of sufficient size to strongly interact with light. We demonstrate a method to synthesize mesoporous Au NPs with large, tunable pores. L-Cysteine acts as a metallogelator to form a dense, less mobile Au(I)−thiolate precursor that traps aggregated block copolymer micelles and facilitates the reduction of mesoporous Au NPs. Electron tomography measurements showed that the pores were distributed throughout the interior and exterior of the particle. Electrochemical methods were used to estimate the chemical reactivity of the surface active sites and estimate the accessible surface area of the pores to ensure that the metal surfaces were maximally accessible to the environment. The 3D models generated by tomography were then used to simulate their optical properties. Mesoporous Au NPs support multipolar plasmon resonances that penetrate deep into the interior pores of the NP. A simple model indicates that porosity affects the local optical conductivity of the NP by subdividing it into tiny nanoscale junctions that redshift the plasmon modes without changing the overall size or shape of the NPs. Large pores promote symmetry breaking, causing the quadrupolar and dipolar modes to overlap and form strongly hybridized plasmon modes. In the context of photocatalysis, porosity-induced symmetry breaking is advantageous because strong electric fields of the plasmon are colocalized along concave/convex features where step-edges and kinks in the atomic structure generate numerous catalytic active sites. Plasmon-enhanced photodegradation of metanil yellow was used to demonstrate the superior photocatalytic properties of meso Au NPs versus nonporous Au NPs.

■ INTRODUCTION

The ability to control both the exterior surface and interior voids of nanomaterials is important because surfaces and open spaces create unique physicochemical properties and increase the utilization efficiency of materials. Mesoporous chemistry has been used to create pores in materials such as silica,[1,2] metal oxides,[3,4] carbon,[5,6] and metals[7,8] that have enhanced properties in diverse applications in drug delivery,[9] electrochemistry,[10] biosensing,[11] optics,[12] theranostics,[13] and energy storage.[14,15] Adding pores in metals has three main advantages: (i) the pores create convex/concave surfaces that expose and help stabilize low coordination surface atoms.[16,17] The presence of unsaturated metal atoms and high index facets can enhance the activity and selectivity of metal surfaces in catalysis.[18] (ii) Pores in metal impose electromagnetic (EM) boundary conditions that generate intense and highly contorted EM fields via surface plasmon resonances. For example, core−shell Au NPs containing dielectric cores support complex multipolar modes,[19] and arranging them into clusters can create artificial magnetism and sharp resonances with highly localized EM fields.[20] (iii) Pores create pathways for mass and thermal transport. Pores strongly influence electrocatalytic activity by enabling guest molecules to move from the outer part to the inner part of the porous structure.[21]

Au is an important metal in electrocatalysis and optical applications due to its favorable electronic properties and chemical stability.[22−25] Numerous methods have been developed to create porous Au nanostructures, including dealloying,[26] galvanic replacement,[27] and various kinds of hybrid templating approaches.[28,29] Templating methods use materials including SiO_2 nanospheres,[30] polymeric particles,[31] polymer micelles[32] to direct the growth of the metal sublattices as it grows into a mesoporous structure. We previously developed a colloidal method to create ultra-large pores in

Received: April 13, 2022
Revised: July 4, 2022
Published: August 12, 2022

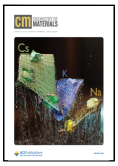

https://doi.org/10.1021/acs.chemmater.2c01125
Chem. Mater. 2022, 34, 7256–7270

various transition and coinage metals using chemical reduction in the presence of block copolymer micelle (BCM) pore-directing agents.[33] This method is unique because it is compatible with metal and nonmetal alloys with vastly different surface energies, including Rh,[34] PdCu,[35] and *a*-CoB_x.[36] The method is mainly driven by kinetics, which is particularly advantageous in multicomponent reactions because the constituent materials tend not to phase separate. The BCMs are removed by washing with an appropriate solvent or thermal treatment to expose the surface of the porous network. BCMs are composed of polystyrene (PS) and polyethylene oxide (PEO) blocks that form highly stable micelles due to the opposing, segregated intramolecular forces associated with the hydrophobic PS core and hydrophilic PEO shell. Continuous compression of the PS core by the polar environment provides structural integrity, while the PEO shell stabilizes the micelles in solution and allows the BCMs to interact with metal precursors.[37,38] PS-*b*-PEO BCMs can have much larger diameters than molecular surfactant micelles and are stable over a wide range of solvent parameters, and their diameters can be tuned via swelling with a cosolvent.[39] BCMs are good templates for growing porous metals because they can be removed by using solvent or heat treatment to expose the interior metal surfaces of the metal architecture. However, making mesoporous Au NPs has been challenging because solvated Au^{3+} cations have relatively high mobility and significant positive reduction potential. As a result, encapsulating BCMs is difficult and chemical reduction tends to form low surface energy morphology NPs that are convex and nonporous.

A significant advance in creating mesoporous Au NPs was recently made by templating them with thiol-terminated $C_{22}N$-SH amphiphilic micelles.[40] Thiol-bearing molecules have long been used in the Au nanocluster field as metallogelators that convert Au(III) precursors into supramolecular assemblies of Au(I) thiolates before reduction and the formation of the Au cluster.[41−43] Metallogelation has the side effect of lowering the mobility of Au via the Au(I)−thiolate complexes and helps the Au metal precursor form and condense around the micelles before reducing the Au(I) thiolates into Au^0. However, micelles using molecular surfactants have limited sizes, so the maximum pore diameter using $C_{22}N$-SH was ~5 nm. The optical extinction properties of a mesoporous Au NP with 5 nm diameter pores are not significantly different from a nonporous Au NP at visible wavelengths because the mesoporous features are too small to induce significant anisotropy or disorder in the optical medium. Thus synthesizing Au NPs with larger pores is necessary to affect the local surface plasmon resonance (LSPR) modes of the NP and expose their interior metal interfaces to the environment where they can participate in plasmon-based chemistry.

Creating BCMs bearing thiol functional groups is not an ideal solution for making pores in Au NPs because the surface density of the thiol groups would not be significant and eventually cause the polymer to be less stable over time. However, recently other research groups were using Au and L-cysteine (L-Cys) to make complex, free-standing 1-D and 2-D nanostructures over a wide temperature and pH range via Au(I)−thiolate bonds.[44] Therefore, we proposed a hybrid approach where we remove the thiol group from the pore-forming agent like in Lv, et al.[40] and delegate Au(I)−thiolate bond formation to a separate molecule like L-Cys. Then the Au(I)−Cys metallogelate network could physically trap the BCM pore forming agents to make mesoporous Au NPs. This paper describes a process to implement thiol ligands in soft-templating reactions with BCMs to synthesize mesoporous Au NPs with ultra-large tunable pores and test their electrocatalytic, optical, and photocatalytic properties. We explain how pores break the symmetry of plasmon modes and create strongly localized hybridized plasmon modes in an ultrahigh surface area morphology that is advantageous for plasmon-driven phenomena including photocatalysis.

■ RESULTS AND DISCUSSION

Synthesis of Mesoporous Au NPs. Mesoporous metal NPs synthesized with BCMs typically follow this general procedure:[16,39,45] the PS-*b*-PEO diblock copolymer is initially dissolved in tetrahydrofuran (THF). This solution should be clear, indicating that the PS-*b*-PEO is dissolved as a unimer. Then metal precursor and some cosolvents like ethanol and water are added, causing the solution to become cloudy due to the assembly of the PS-*b*-PEO polymer chain into BCMs with sufficient light scattering ability. Finally, the reducing agent is added to the mixture, causing the solution to transform in color as the metal is reduced to form the NPs. Then the product is separated from excess reagents via consecutive cycles of washing/centrifugation. Eventually, the final product is imaged with scanning electron microscopy (SEM) to evaluate the porous structure. This procedure works with various metals with minor modifications, but it has failed to generate mesoporous Au NPs until now. BCMs cannot be embedded into the growing Au NPs under these conditions. Instead, the Au aqua-complexes tend to reduce and form nonporous Au NPs (Figure S1a). Therefore, we experimented with different small molecules with thiol groups such as *p*-mercaptobenzoic acid, glutathione, and L-Cys to generate lower-mobility Au(I)−thiolate intermediates before reduction to the metal. By delegating Au−thiolate formation to thiol molecules, the main role of the BCM is to serve as a steric barrier and create open spaces inside the NPs.[46] We also added KOH to the reaction to modulate the kinetics of the reduction reaction, which we will describe in detail later. Aqueous solutions containing Au^{3+} precursor are typically yellow, but once the thiol molecules are added, the solutions become cloudy and yellow, indicating Au(I)−thiolate formation. To implement Au(I)−thiolates into the BCM synthetic method, the standard method can be followed where Au^{3+} precursor is added to THF/ethanol containing PS-*b*-PEO. Then KOH and the thiol molecules are added to form the Au(I)−thiolate metallogel. The metallogel is then reduced by adding aqueous AA to the solution. For the reaction with L-Cys, the solutions appeared blue within ~5 s and eventually became red-blue after ~30 s, while the final product using other thiol molecules was black. The products were then centrifuged, washed, and imaged in SEM. Figure S1b−d shows the products generated using three thiol molecules: L-Cys, glutathione, and *p*-mercaptobenzoic acid. Only L-Cys created mesoporous Au NPs, whereas the other ligands generated nonporous aggregated Au NPs. In nanocluster synthesis methods, bulkier ligands tend to impart better stability to Au nanoclusters.[47] However, intermediates with high stability are not as desirable in mesoporous templating reactions because the organic ligands must ultimately be displaced for significant metallization to proceed. It has been reported that glutathione and *p*-mercaptobenzoic acid have been used for the synthesis of highly stable Au nanoclusters because bulky ligands can

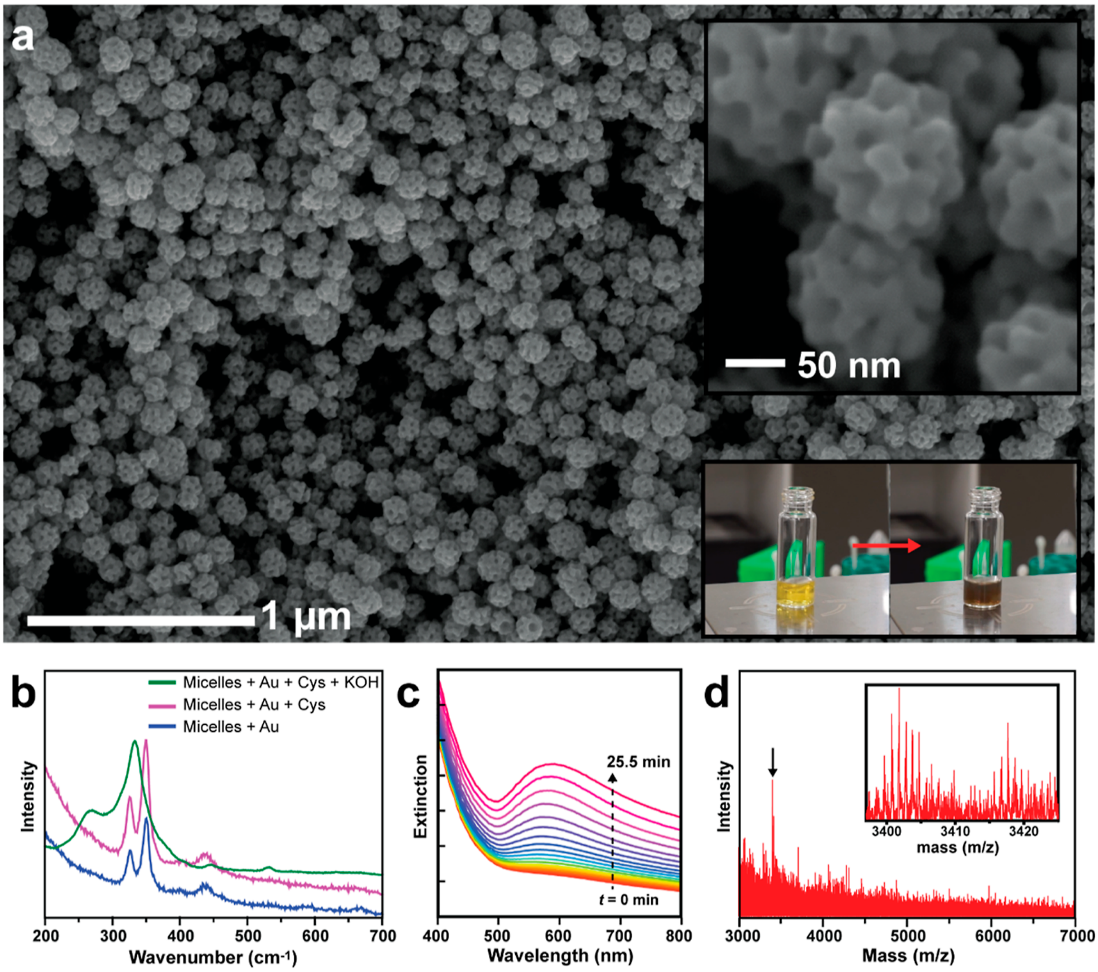

Figure 1. Mesoporous Au Nanoparticles. (a) SEM micrograph shows that the Au particles are relatively uniform in size. The surface of each particle is riddled with tiny pores (inset; top). When KOH is added to the reagent solution, the solution turns from yellow (t = 10 s) to dark brown (t = 120 s), indicating the formation of nanoclusters (inset; bottom). (b) Raman spectra were collected as reagents were added to the reaction solution containing BCMs. The characteristic Raman spectrum of $HAuCl_4$ shifted to lower frequencies and broadened upon the addition of KOH. (c) Time-dependent UV−vis absorbance spectra were collected over time (t = 0 to 25.5 min; increment 1.5 min) to examine the formation of NPs. Both PS-*b*-PEO and the AA reducing agent were omitted from the solution, yet the Au precursor [19.3 mM] was still reduced by L-Cys [1.63 mM] upon the addition of KOH [63 mM]. (d) Positive-ion mode MALDI-TOF mass spectra of the as-prepared samples from the mixture solution containing solvent, L-Cys, KOH, and $HAuCl_4$.

promote steric effects.[48,49] Therefore, they are not suitable for this system because stable Au nanoclusters inhibit the growth of crystalline Au metal around the BCMs. We speculate that L-Cys works best in this reaction because it is less bulky and has some ambidexterity because its amine, carboxylic acid, and thiol groups can bind/unbind to Au surfaces depending on the changing chemical environment.

The as-synthesized mesoporous Au NPs prepared with L-Cys were then examined with SEM to measure their average exterior dimensions. Figure 1a shows that the obtained mesoporous NPs are well-dispersed and appear highly uniform in shape and size. The average diameter of this sample was estimated to be 120.2 ± 9 nm after analyzing >200 NPs (Figure S2). SEM imaging revealed that the surfaces of the particles are decorated with abundant pores with a narrow size distribution of 18.3 ± 2 nm and pore walls with thicknesses of 17.3 ± 2 nm (Figure S3a,b). Small-angle X-ray scattering (SAXS) was used to measure the periodicity of mesoporous Au NPs and estimate the pore-to-pore distance of the mesoporous Au structure (Figure S3c). The SAXS measurements have a broad peak at 0.204 nm^{-1}, corresponding to a pore-to-pore distance of 32 nm. This observation is consistent with the abovementioned pore size and pore wall thickness (i.e., 18.3 + 17.3 = 35.6 nm). In addition, Figure S4 shows that the polymeric micelles were formed in solution, implying that the pore structure is an inverse replica of the spherical polymeric micelle. The resulting pore diameter is slightly smaller than the size of polymeric micelles observed by TEM (∼24 nm). The difference in size is caused by the overgrowth of Au crystal around BCMs, which tends to slightly shrink the pore size. The same results were previously reported when mesoporous PdCu was prepared with PS-*b*-PEO BCMs.[35] The synthesis mechanism was examined using a combination of UV−vis absorption spectroscopy and Raman spectroscopy to identify any changes as PS-*b*-PEO, $HAuCl_4$, L-Cys, and KOH reagents are added in sequence. In the UV−vis spectra (Figure S5a), most solutions containing $[AuCl_4]^-$ have an absorbance peak at λ = 325 nm associated with the ligand−metal charge transfer. The shoulder peak at lower energies corresponds to the d-d transition of the $[AuCl_4]^-$ square planar ion. In the presence of KOH, the UV−vis peak at 325 nm is severely attenuated, indicating a chemical reaction and change in the

Au^{3+} coordination sites. Interestingly, Au nanoclusters formation seems to occur after the addition of KOH, as the color of the solution becomes black and turbid. Wavelengths <300 nm cannot be measured due to the strong absorption of the solvent in this region. Figures 1b and S5b show the Raman spectra of the same solutions. $[AuCl_4]^-$ ions have Raman peaks at 350 and 326 cm^{-1} due to symmetric (A_{1g}) and antisymmetric stretching (B_{1g}) modes, respectively. Even when L-Cys is added to the reaction mixture, there is little change in the Raman spectrum. However, the Raman spectrum changes quite drastically upon the addition of KOH, and two Raman peaks at ~333 and 265 cm^{-1} emerge. Strongly basic conditions will deprotonate all L-Cys ligands to form the thiolate anion (RS^-). Then the thiolate anion can readily interact with the Au precursor to form oligomeric or polymeric $[Au^I\text{-}SR]_x$ complexes.[41,50] Researchers have examined the Raman vibrations of monomeric RS-Au^I-SR and dimeric RS-Au^I-SR-Au^I-SR structures on the surface of Au clusters.[51] These motifs generate Raman bands in the 250−350 cm^{-1} range that are associated with Au−S stretching. In Figure 1b, the 333 and 265 cm^{-1} Raman bands created upon the addition of KOH match the radial vibrations of $[Au^I\text{-}SR]_x$ in Au clusters versus other potential moieties; thus, we assume that the addition of KOH creates polymeric Au complexes and even some Au clusters or particles capped with L-Cys. The interaction between Au and L-Cys in basic conditions was monitored over time in the absence of PS-*b*-PEO and AA using UV−vis spectrophotometry. Interestingly, the UV−vis data (Figure 1c) indicates that the Au precursor [19.3 mM] was reduced by L-Cys [1.63 mM] in the presence of KOH, as can be seen in the gradual increase of the absorption peak at ~580 nm. The solution appeared black (inset Figure 1a), which is a signal that tiny Au NPs or clusters have been formed. This observation is consistent with other reports showing that peptides with cysteine residues can form Au clusters.[52,53] Indeed, metal nanoclusters have even been prepared using L-Cys as a reducing agent.[54,55] KOH strongly regulates the reaction, and sufficient basicity is essential to enhance the reducing capability of L-Cys (Figure S6), as noted in related studies.[56−59] The abovementioned solution was collected and measured in high-resolution TEM (HRTEM) (Figure S7). HRTEM shows that tiny <2 nm diameter Au NPs form in the absence of AA and PS-*b*-PEO. The size of these particles could be smaller but likely aggregate due to the 200 kV electron beam in TEM. In addition, matrix-assisted laser desorption/ionization-time-of-flight (MALDI-TOF) analyses of the above-mentioned solution show the presence of molecules with masses ~3417 and ~3401 Da, indicating that small Au nanoclusters are present upon the addition of KOH (Figure 1d). Also, washed samples have XPS peaks for Au(I) and Au(0)[60] (Figure S8), and EDX can detect a small amount of sulfur (Figure S9) indicating that the particles are capped with Au(I)−Cys sites.

Control experiments were performed to study the role of each component in the synthesis process. L-Cys impedes the random growth of Au; however, the porous framework fails to form without the presence of BCMs (Figure S10a). The omission of KOH results in large 2.5 μm diameter particles (Figure S10b). These results combined with earlier observations indicate that KOH increases the reducing power of the solvent and, thus, increases nucleation, which will decrease the final size of the NPs. Considering all of the data together, we concluded that the formation of mesoporous Au NPs proceeds as follows (Figure 2a). Aqueous solutions initially drive PS-*b*-PEO to form core−shell BCMs in solution (Figure 2b,c). Then L-Cys causes the Au(I)−thiolate to form and associate with the surface of the BCMs. KOH destabilizes the Au(I)−thiolate and then clusters form on the outside shell of the BCMs (Figure 2d). Figure S11a shows both the growing mesoporous Au NPs and the Au-capped micelles. Finally, AA triggers the aggregation of the micelles and overgrowth as they begin to form the mesoporous Au NPs in Figure 2e. Figure S11 shows that the SEM images recorded from the samples collected at different reaction times correlate well with the proposed mechanism. This method is conceptually different than methods that use thiol-terminated C_{22}N-SH amphiphilic micelle templates[40] because the metallogelation reaction is independent of the BCM. Hence the pore size of the Au NPs can be increased or decreased by changing the number and ratio of homopolymer subunits (e.g., PS) using a wide range of commercially available BCMs.[33]

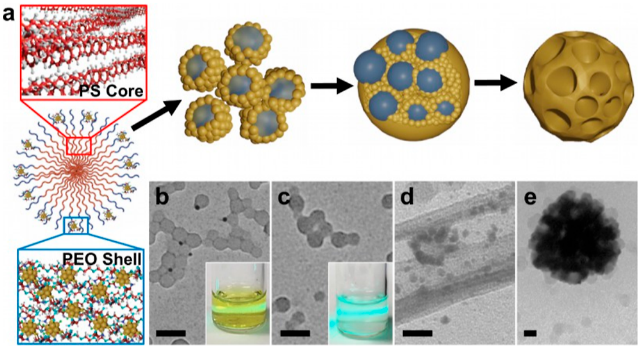

Figure 2. Synthesis procedure for mesoporous Au NPs. (a) Proposed mechanism for the assembly of mesoporous Au NPs using BCMs as sacrificial templates. L-Cys and KOH initiate gelation of the Au precursor and the formation of clusters that adsorb inside the PEO shell of the BCMs. They cause the BCMs to aggregate and form mesoporous NPs with metals that are chemically sintered together with the aid of the AA reducing agent. The BCMs are removed with mixed solvents of ethanol/THF to reveal mesopores in the metal NPs. (b,c) TEM images of $PS_{18,000}$-*b*-PEO_{7500} micelles formed in an aqueous solution (b) with $HAuCl_4$ and (c) without $HAuCl_4$. The black dots in (b) are Au nanoparticles formed by the reduction of $HAuCl_4$ with the electron beam. The emergence of scattering by the micelles via the Tyndall effect is shown in the inset. (d) TEM image of a BCM at the earliest stages of the reduction process as Au NPs surround the spherical micelle. (e) TEM image of mesoporous Au NPs in the presence of BCMs. (b,c) Scale bars, 50 nm. (d,e) Scale bars, 20 nm.

All observations of the reaction indicate that three main variables can be optimized: (i) choice of an appropriate molecular ligand for Au. Thiol ligands modulate the kinetics of nucleation,[55] in addition to directing crystal growth. Of the thiol molecules we tested, L-Cys seems to satisfy these criteria best, but there may be additional molecules that will work. The concentration of L-Cys used in the reaction is also critical. As shown in Figure S12a, reactions deficient in L-Cys [1 mM] cannot promote the formation of mesoporous Au NPs because there are insufficient ligands to bind all Au^{3+} and generate the Au(I)−thiolate. This free Au^{3+} is too mobile and does not associate with the PEO moieties of the BCMs. Thus, encapsulation of the BCMs does not occur. By increasing the concentration of L-Cys [5 mM], the low-mobility of Au(I)−thiolate becomes sufficient for interacting with the

BCMs, which in turn form ~100 nm sized particles with irregular pores (Figure S12b). Compared to reactions with the same KOH concentration, particles with larger diameters and interconnected pore walls can be obtained from the higher concentration of L-Cys [10 mM] (Figure S12c). Thus L-Cys mainly affects nucleation by creating less mobile, dense Au(I)−thiolate intermediates that can be reduced with AA. Higher L-Cys concentrations are necessary to decrease the self-nucleation of the precursor and provide adequate time for Au(I)−thiolate to fully encapsulate the BCMs. (ii) The use of KOH to increase the pH value of the solution favors the destabilization of the Au(I)−thiolate and the formation of nanoclusters. The pH sensitivity of the reaction enables modulation of the reducing power of the reaction and NP size control.[61] Careful control of pH concentration determined the final size of the mesoporous Au NPs (Figure S13a−c) and reactions with [KOH] from 37.2, 40.0, and 42.9 mM resulted in mesoporous Au NPs with average sizes of 230.2 ± 27, 180.7 ± 18, and 120.2 ± 9 nm, respectively (denoted as meso-Au230, meso-Au180, and meso-Au120, respectively) (Figure S13d−f). Figure S14 demonstrates that changing the pH concentration to control the size of the porous particle can also be carried out with a different base. (iii) The concentration of AA chemical reducing agent. AA is a mild reducing agent frequently used in seed-mediated NP synthesis methods because it cannot readily reduce Au^{3+}. Hence AA mainly participates in nanocrystal growth because it cannot easily nucleate the $AuCl_4$ starting material under mild conditions. Figure S15 shows experiments using different reducing agents.[62] AA mainly affects how the Au forms around the BCM template by reducing Au(I)−thiolate or helping sinter the NPs together via some form of oriented attachment. Insufficient AA concentration impairs micelle encapsulation, allowing the BCMs to escape into the solvent and resulting in nonporous facetted Au particles with minimal energy surfaces relative to the porous structure (Figure S16).

3D Morphology of Mesoporous Au Nanoparticles. TEM images confirm that the porous network extends throughout the NP to create a 3D open network (Figure 3a). HRTEM on a highly magnified domain near the edge of the particles has lattice fringes associated with {220} diffraction planes (d = 0.14 nm) of the *fcc* Au lattice (Figure 3b).[63] The thorough observation of HRTEM combined with the XRD pattern (Figure S17) of the sample further confirms that the porous structure is composed of highly crystalline Au metal. Step and kink sites associated with low-coordinated atoms were observed on the periphery of the particle (Figure S18). These unsaturated atomic structures are promising active catalytic sites known to boost electrocatalytic activity in metal electrodes.[64,65] To visualize the internal structure of the mesoporous Au NPs, STEM-HAADF-tomography was used to create 3D model structures for meso-Au120, meso-Au180, and meso-Au230 (Figure 3c−e). The interior space of the NPs can be observed as semi-ordered interconnected pores that extend throughout the metal structures. As the overall particle size increased, there was no collapse in the structure, indicating that the micelles and metal precursor conucleate and grow outward as more metal and micelles are added to the growing particle which is controlled by pH. However, as seen in the 120 nm diameter sample, there are limits to the number of BCMs that a single particle can accommodate. Thus smaller size BCMs are required for making spherical pores in sub-100 nm mesoporous NPs.

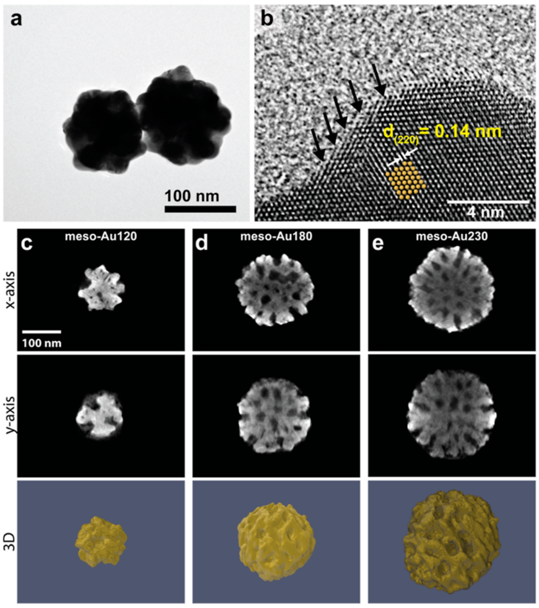

Figure 3. Structural characterization of mesoporous Au NPs synthesized with $PS_{18,000}$-*b*-PEO_{7500} BCMs. (a) Bright-field TEM image of mesoporous Au NPs. (b) HRTEM image of the edge of a pore. STEM-HAADF tomography of mesoporous Au NPs with different particle sizes: (c) 120, (d) 180, and (e) 230 nm. Cross sections were taken from the *x*-axis (top row) and *y*-axis (middle row). The 3-dimensional models of each particle are shown in the bottom row.

Estimating Reactivity and Accessibility of Au Pores via Electrochemistry. Electrochemistry is a well-known application for mesoporous metal architectures. However, electrochemistry can also be used as a tool to study the structural properties and surface area of porous architectures via the reactivity of the active sites and the electrochemical active surface area (ECSA). We initially examined the performance of the mesoporous Au NPs for the ethanol oxidation reaction (EOR) because the porous structure increases the surface area of the NP and the convex/concave shape of the pores exposes unsaturated metal atoms that can participate as active sites in catalytic reactions. Quasi-spherical Au NPs with the equivalent size were also prepared as a control structure and evaluated alongside the mesoporous Au NPs (Figure S19). Figure 4a shows the ECSA data for mesoporous Au NPs (120 nm) with the nonporous quasi-spherical Au NPs (denoted as nonporous Au120) generated using cyclic voltammetry (CV) in 0.5 M H_2SO_4 at a scan rate of 50 mV s^{-1}. The CV curves from meso-Au120 and nonporous Au120 possess a pair of peaks in the forward scans from 1.0 to 1.5 V Ag/AgCl) and in the backward scan from 1.2 to 0.75 V (vs Ag/AgCl). They correspond to the characteristic of the Au electrode where the broad anodic peak in the forward scan is ascribed to the formation of the Au oxide layer and the second peak in the backward scan indicates the reduction of the oxide layer. The mass-normalized ECSA of meso-Au120 is estimated to be 6.1 m^2 g^{-1}, which is higher than that of nonporous Au120 (1.2 m^2 g^{-1}) (inset Figure 4a), and this value is comparable to the porous Au NPs that have been reported previously.[28,29] This enhancement suggests that the meso-Au120 NP has more exposed catalytic active sites than smooth nonporous Au120 NPs. Furthermore, electrocatalytic oxidation of ethanol was performed to probe the electro-

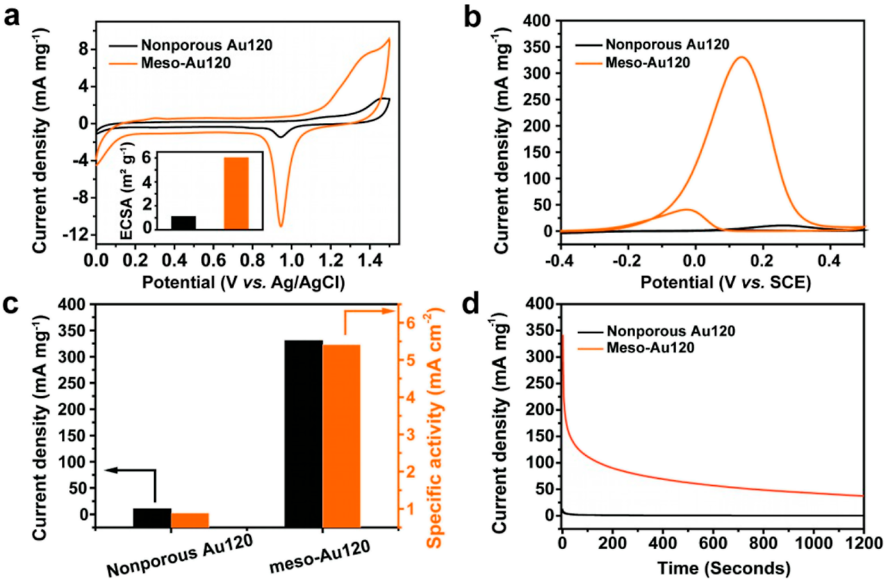

Figure 4. Electrocatalytic performance of mesoporous Au NPs versus nonporous Au NPs. (a) CV curves of the meso-Au120 and nonporous Au120 NPs in 0.5 M H_2SO_4 with the scan rate of 50 mV s^{-1}, and the corresponding ECSA (inset). The catalytic ethanol electrooxidation measurements in the form of (b) cyclic voltammograms in 1 M NaOH and 1 M CH_3CH_2OH with the scan rate of 50 mV s^{-1}, (c) summary of mass and specific activities over EOR, and (d) *i*−*t* curves of meso-Au120 and nonporous Au120 NPs at potentials of 0.12 and 0.25 V, respectively.

catalytic activity and stability of the meso-Au120 and nonporous Au120. There are two peaks in the CV curve with 1 M ethanol and 1 M NaOH solution (Figure 4b) that exhibit the characteristic behavior of the Au electrode for EOR. For meso-Au120, the broad oxidation peak with the maximum current density of 331.2 mA mg^{-1} at 0.13 V is observed in the forward scan ranging from −0.3 to 0.4 V, which can be attributed to the four-electron transfer of ethanol electrooxidation.[66,67] In the backward scan, the second anodic peak is located at −0.02 V, indicating a reduction of the hydroxy layer of Au and thorough removal of the intermediate carbonaceous species formed during the forward scan. On the other hand, the peak potential of the nonporous Au120 is observed at a more positive potential of 0.26 V with a peak current density of 10.8 mA mg^{-1}. The result demonstrates that the as-prepared Au NPs with porous architectures possess a mass activity ~31 times higher in electrocatalytic performance of EOR compared with its quasi-spherical counterpart. The specific activity of 5.41 mA cm^{-2} from mesoporous Au NPs is also higher than that of the nonporous Au NPs with 0.88 mA cm^{-2}, indicating that highly active sites are more exposed (Figure 4c). Poisoning of active sites by intermediate carbonaceous species is a significant problem in EOR. The ability of a catalyst to resist poisoning can be measured using the ratio of peak current densities for the forward and backward anodic peaks (I_f/I_b)—a larger ratio indicates a higher resistance.[68] Nonporous Au120 and meso-Au120 NPs exhibited an I_f/I_b of 5.7 and 8.1, respectively. The result demonstrates that the meso-Au120 NPs outperform nonporous Au120 in oxidizing the intermediate carbonaceous species.

Chronoamperometry (CA) was employed to evaluate the stability of the mesoporous Au catalysts in the EOR (Figure 4d). The current−time response was recorded at 0.12 and 0.25 V for meso-Au120 and nonporous Au120, respectively. The current density of meso-Au120 and nonporous Au120 decrease at the beginning of the measurement and then reach a steady state after 1200 s. The blocking of active sites likely causes this gradual deterioration due to the accumulation of carbonaceous species.[69] The meso-Au120 exhibited slower deterioration with the steady-state current density of 40 mA mg^{-1}, whereas the currents of nonporous Au120 significantly diminished to 0.3 mA mg^{-1}. This result is in good agreement with the tendency of meso-Au120 to resist poisoning in EOR more effectively. Accordingly, the meso-Au120 shows superior electrocatalytic performance to the quasi-spherical Au nanoparticles. For comparison, the reported catalysts for EOR are listed in Table S1. The as-prepared meso-Au120 is even outstanding versus other Au-based catalysts. This observation implies that the synthetic method creates structures with 3D interconnected pores that enable good mass and electron transfer properties while exposing numerous low-coordinated atoms for catalysis.

ECSAs of the three batches of particles (i.e., meso-Au120, 180, and 230) were measured to determine if the interconnected and accessible porous network is maintained as the particles increase in size. Figure S20a shows the CV curves from the gold oxide striping of all mesoporous Au samples. The calculated ECSA for meso-Au decreased with the increase in particle size, which was 6.1, 5.7, and 5.4 m^2 g^{-1} for meso-Au120, meso-Au180, and meso-Au230, respectively (Figure S20b). Thus, the smaller particles with the porous architecture will provide a larger surface area for catalysis. ECSA allows us to roughly estimate the surface area of single particles and compare them to the total surface area provided by the tomography models (see Note S#1). Tomography models provide an upper bound of surface area because all surface areas, even inaccessible pores, can be measured. The ECSA indicates that the mesoporous particles have more surface area than hard spheres and a large proportion of their pores are accessible. Figure S21a displays the characteristic CV of ethanol electrooxidation and particle size-dependent EOR of mesoporous Au NPs. The apparent tendency of peak potential and the corresponding current density over the size of particles are observed. In the forward scan, the peak potential shifts from 0.13 to 0.15 V as the size of the particles increase from 120 to 230 nm. This observation indicates that the process of ethanol electrooxidation was more easily triggered on

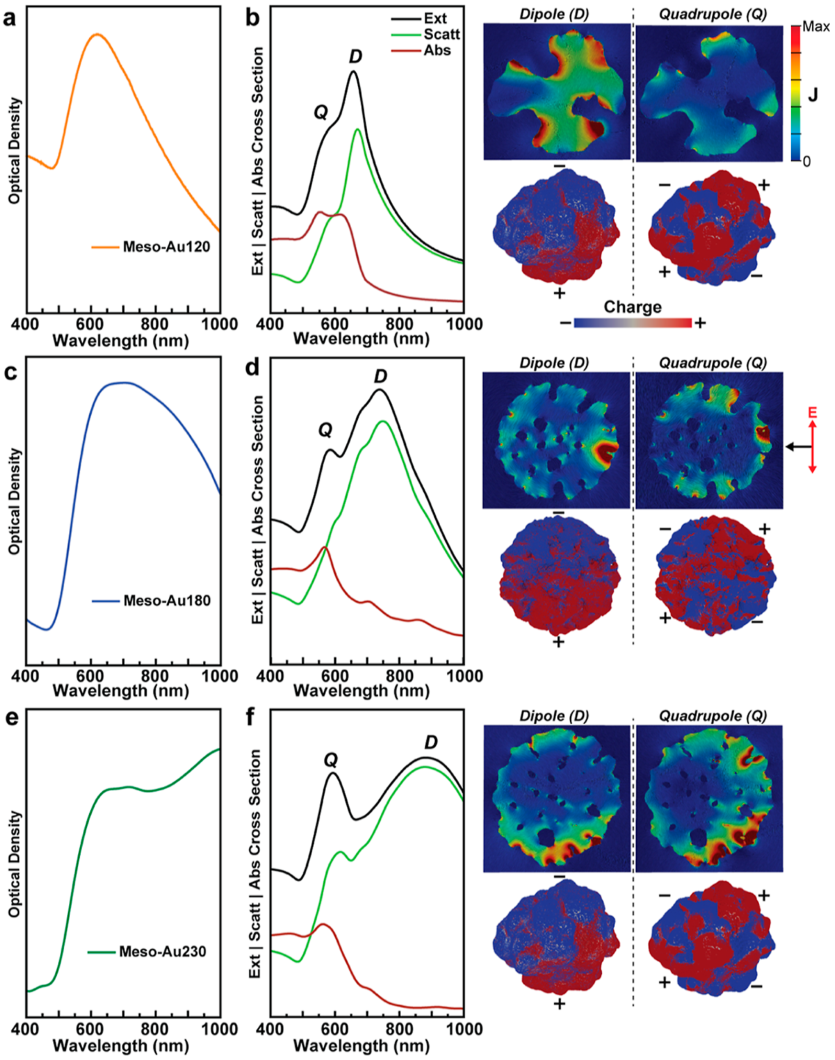

Figure 5. Experimental and simulated optical properties of mesoporous Au NP samples synthesized with $PS_{18,000}$-*b*-PEO_{7500} BCMs. The overall diameter of the particles was 120 nm [(a,b) meso-Au120], 180 nm [(c,d) meso-Au180], and 230 nm [(e,f) meso-Au230]. The UV–vis spectrophotometry measurements (a,c,e) show that the plasmon resonance redshifts as the size of the particle increases. The tomography structures shown in Figure 3 were input into a computational electrodynamics code to model their extinction, scattering, and absorbance cross sections (left b,d,f). Peaks in the spectra were examined using their current density map bisecting the center of the NPs (b,d,f right top) and 3D surface charge map (b,d,f right bottom) to identify the dipolar (D) and quadrupolar (Q) modes. In the simulated maps, light is incident from right to left and the polarization of the electric field is parallel to the page.

mesoporous Au NPs with smaller diameters. In addition, the easier ethanol electrooxidation takes place on the smaller particles of meso-Au is also confirmed by the increase of current density as the size of the particle decreases. The current density of meso-Au120, meso-Au180, and meso-Au230 are 331.2 mA mg^{-1} (5.41 mA cm^{-2}), 295.9 mA mg^{-1} (5.23 mA cm^{-2}), and 270.4 mA mg^{-1} (5.18 mA cm^{-2}), respectively (Figure S21b). The stability test of EOR performance also suggests that the more stable and higher steady-state current density of EOR can be achieved with the smaller size of mesoporous Au particles (Figure S21c). Smaller mesoporous Au NPs have higher electrocatalytic activity because they exposed more concave/convex surfaces that supported numerous low-coordinated atoms that are good active sites. This result further indicates that the high controllability of size without compromising the porous features can be effectively achieved via careful control of KOH concentration, hence, providing a higher number of active sites when the particle size is smaller. Linear sweep voltammetry measurements at various scan rates were also carried out to examine the mass transfer properties of the mesoporous Au NPs with different sizes of particles for EOR. As shown in Figure S22a−c, the peak current density of EOR by all catalysts increases with the increasing scan rate. In addition, the peak current densities for all samples have a linear relationship with the square root of scan rate (Figure S22d) showcasing that the EOR by mesoporous Au NPs is a diffusion-controlled process.[70,71] In this case, the diffusion efficiency of each catalyst is represented by the slope. As the slope value increases with the decrease of the size of the particle, it suggests that the electron and mass transfer on the mesoporous Au NPs is improved when the size of the particle is smaller.[70] This result accounts for some of the increase in the catalytic activity of the smaller diameter mesoporous Au NPs.

Characterizing the Optical Properties of Mesoporous Au Nanoparticles. The optical properties of metal nanostructures with subwavelength voids, holes, and gaps have long been a topic of fascination because nanoscale noble metals

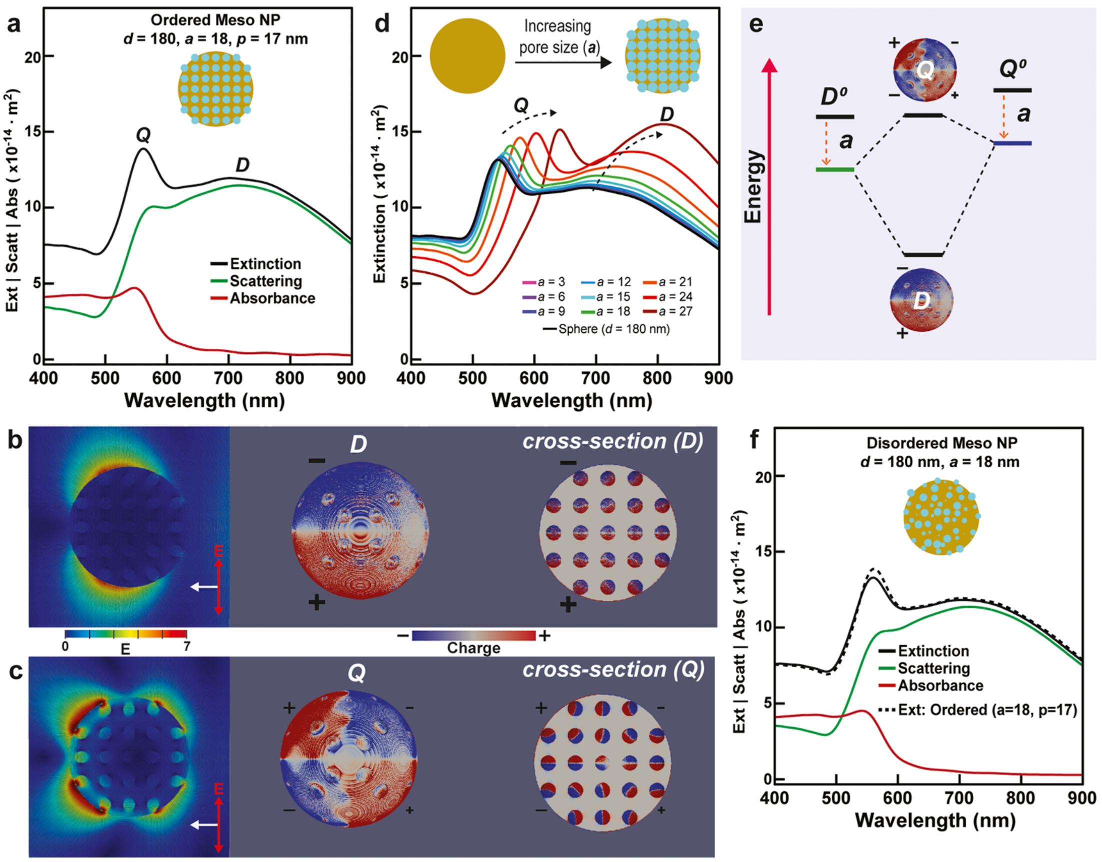

Figure 6. Simulated optical properties of a 180 nm diameter Au NP as pores are added to the structure. (a) Extinction, scattering, and absorbance cross sections for a single 180 nm diameter spherical Au NP perforated with a bcc array of 18 nm diameter pores spaced by 17 nm. The particle supports a dipolar (D) and quadrupolar (Q) resonance. Electric field maps (left) and 3D charge polarization maps (middle, right) for the D resonance (b) and Q resonance (c). A charge is piled up on the left side of the D-resonance, causing it to overlap spatially and hybridize with the Q-resonance. The cross section of the polarization maps (right) shows that even the surfaces of the interior pores are polarized toward the overall polarization of the mesoporous Au NP. (c) Diameter of the nanoparticle and pore spacing were fixed (i.e., $d = 180$ nm and $s = 17$ nm) and the diameter of the pores (a) was varied from 0 to 27 nm in 3 nm increments. Increasing pore size causes the Q and D modes to redshift. (d) Redshift can be explained in part by symmetry breaking and plasmon hybridization theory (e). Spherical NPs support primitive D^0 and Q^0 modes. Increasing pore size causes the D^0 and Q^0 modes to spatially overlap and hybridize, forming antibonding Q and bonding D modes. A similar phenomenon can be observed by increasing the diameter of solid Au NPs (see Figure S24). (f) Extinction, scattering, and absorbance cross sections of a 180 nm diameter Au NP perforated with a random arrangement of $a = 18$ nm diameter pores. The extinction of the NP with ordered pores was included for comparison showing that ordering has minimal impact on LSPR.

support collective excitations of free electrons called surface plasmons that can focus and manipulate light.[72] For example, early research in plasmonics showed that light could couple to surface plasmons in metal films and travel through subwavelength holes.[73,74] Also, dielectric cavities in the center of core−shell Au NPs create tunable multipolar modes.[19] Arranging NPs into electrically capacitive clusters generate collective broad-band hybridized modes.[20,75] Additionally, concave and convex metallic features are capable of collecting and focusing light.[76,77] Mesoporous Au NPs are relevant in this context because they combine all of these aspects into an analogous structure, but one that is conductive instead of capacitive. Researchers working on mesoporous chemistry have briefly explored the optical properties of mesoporous metals. For example, etched and dealloyed porous metal NPs support LSPRs that enhance Raman scattering[78] and the local electric field intensity.[26] However, no work has studied how arrays of pores affect the optical extinction properties and wavelength-dependent plasmon modes of mesoporous NPs. At the very least, pores should affect the optical conductivity of the structure and enable one additional degree of freedom besides size and shape to tune the plasmon resonance of the particles.

We took the three 3D models in Figure 3c−e and input them into a computational electrodynamics solver (Lumerical Solutions). The model used polarized plane-wave excitation and the Au material was modeled using the optical constants described by McPeak,[79] and the pores and background were set to a refractive index of 1.333. For reference, we collected the UV−vis spectra for each batch of particles from which the particles were taken (Figure 5a,c,e). As expected, the plasmon resonance redshifts and broadens as the average diameter of the mesoporous Au NPs in each ensemble solution increases in size from 120 to 180 to 230 nm. The tomography structures in Figure 3 were input into our model to calculate the normalized extinction, scattering, and absorbance cross sections of the corresponding mesoporous Au NP models (left Figure 5b,d,f). The modeled spectra qualitatively match the UV−vis spectra, but the experimental spectra are broader, likely because there is some variation in the size and internal structure of each particle in the ensemble (Figures S2, S3, and S13); additionally, UV−vis spectrophotometry uses unpolarized light which may contribute some broadening as particles are randomly oriented in solution. Meso-Au120 supports a resonance in the location of the UV−vis spectrum (left Figure 5b). Plasmon modes were examined by plotting the current density map and 3D charge polarization. Current density (J) is a useful way to detect regions inside the metal that contribute to the highest electric field enhancement inside the pores. The modeled particle supports strong J that penetrates to the interior of the particle and the charge polarization plots indicate that the particle supports dipolar (D) and quadrupolar (Q) modes (right Figure 5b). The larger meso-Au180 NP and meso-Au230NP both support D and Q modes that also appear to redshift and broaden as the overall diameter of the NP increases (right Figure 5d,f). In all cases, the J plots show that the plasmon affects both the exterior and interior spaces of the structure and enables more surface area of the structure to contribute to the overall electric field enhancement. We synthesized mesoporous Au NPs with roughly the same outer diameter (d = 120 nm) but using BCMs having increasing diameters (p = 12, 18, and 23 nm) using $PS_{10,000}$-b-PEO_{4100}, $PS_{18,000}$-b-PEO_{7500}, and $PS_{63,000}$-b-$PEO_{26,000}$, respectively (Figure S23a−f). The UV−vis spectra of these samples show that the plasmon resonance redshifts and broadens simply by increasing the diameter of the BCM, which proves that porosity is an additional dimension to tune the plasmon wavelength of mesoporous metal NPs while keeping its outer dimensions constant (Figure S23g).

Mesoporous Au NPs have attractive properties for photocatalysis because they possess numerous low-coordinated atoms and have strong scattering and absorbance properties at visible wavelengths. To better understand how porosity affects plasmon modes, we created some simple models of nonporous and porous Au NPs with a fixed d of 180 nm to roughly approximate meso-Au180 (Figure 5c,d). Meso-Au180 was chosen because it had the most distinct pores in tomography and showed E-field penetration to the interior of the particle. First, we simulated the extinction, scattering, and absorbance cross sections of a 180 nm diameter Au sphere perforated with a body-centered cubic (*bcc*) array of 18 nm diameter pores (a) spaced 17 nm edge-to-edge (s) to match the rough dimensions of the meso-Au180 sample (Figure 6a) and reflect the entire ensemble measured in the SAXS data (Figure S3a,b). The model Au NP has two strong peaks at λ = 561 nm and λ = 730 nm. In Figure 6b, we mapped the electric field profile (left), 3D charge polarization map (middle), and 3D charge polarization cross section (right) for the peak at λ = 730 nm. The plane wave excitation source is incident from right to left, and polarization is indicated by the red arrow. The simulations indicate that the peak at 730 nm is a dipolar (D) resonance and that the charge is piling up on the side of the particle furthest away from the source. The 3D cross section shows how the surfaces of the pores are polarized in phase with the overall polarization of the Au NP. The peak at λ = 561 nm appears to be a quadrupolar (Q) mode (Figure 6c) based on its electric field and charge map. The individual polarization of each pore in the Q mode is dipolar and rotated to be in phase with the overall Q mode based on the pore location. Only the pore at the center of the 180 nm diameter particle is quadrupolar. To understand the coupling mechanism, we simulated the same Au NP but with different pore sizes (a = 0, 3, 6, 9, 12, 15, 18, 21, 24, and 27 nm) and fixed pore locations (Figure 6d). Increasing pore size causes the D and Q resonances to redshift; redshifting accelerates and the Q mode increasingly adopts a Fano lineshape as the pores begin to overlap at a = 27 nm. This behavior is similar to the effect of NP size, where increasing the diameter of a spherical Au NP causes the Q resonance to emerge and redshift with the D resonance (Figure S24). Increasing pore size causes symmetry breaking as the particle becomes sufficiently large to experience an electric field with a time-dependent phase. Symmetry breaking is frequently used to obtain plasmon modes with larger local field enhancements due to the asymmetric spatial arrangement of charge in hybridized modes.[80,81]

Porosity also induces symmetry breaking in spherical NPs because it facilitates the emergence of hybridized D and Q modes, which are superpositions of primitive (i.e., unhybridized) dipolar (D^0) modes and quadrupolar (Q^0) modes. Porosity clearly helps precipitate the piling charge in the D mode (Figure 6b; middle), causing it to shift to the aft section of the Au NP and spatially overlap with the Q mode (Figure 6c; middle). We hypothesize that the pores simultaneously affect the energy of the unhybridized D^0 and Q^0 modes by decreasing the overall optical conductivity of the entire structure. Optically induced transfer of charge across conductive junctions shifts the plasmon resonance to lower energies as the metal junction becomes thinner.[82] Figure 6e shows an energy diagram describing the effect of porosity on hybridization. Increasing a creates thinner pore walls, allowing the plasmonic wavefunctions of D^0 and Q^0 to mix and form hybridized bonding (D + Q) and higher energy antibonding (D − Q) modes with highly localized electric fields at visible wavelengths. The D mode is a broad radiant mode, while the Q mode is intrinsically a narrow subradiant mode. Changing a controls the amount that these modes overlap spectrally and causes them to interfere and generate an increasingly narrow Q mode, which is characteristic of Fano resonances. We also observed a similar effect in 120 nm diameter Au NPs perforated an array of pores with the same spacing and varying pore diameter (Figure S25) and observe red-shifting of the D mode and the emergence of a strong Q mode. In addition, the pores inside the as-synthesized particles are not ordered in a perfect bcc array like the simple model in Figure 6a,b. Figure 6f shows the simulated cross sections for a 180 nm diameter particle with randomly distributed 18 nm diameter pores using a similar number of pores as the ordered array (Figure 6a). Interestingly, the location and shape of the D and Q modes are roughly identical in both ordered and disordered pores, indicating that conductive coupling is the primary mechanism and that local optical conductivity dominates the properties of the nanoparticle rather than the periodic spacing of the pores. However, it is worth noting that larger overlapping pores may allow interpore coupling because the length scale of the plasmon would be much larger. Nanoscale junctions and interfaces should impact the lossiness of the plasmon mode, but the magnitude of its contribution to the optical properties in the mesoporous particles prepared in the experiment is unknown. We modeled the 180 nm diameter ordered NP model, shown in Figure 6a, and the tomography-generated meso-Au180 NP using a Drude model (DM) for Au that removed the contribution of interband transitions (Figure S26). Then, we increased the collision frequency of the DM to observe how a reduction in the mean free path of electrons (λ_e) via structure might impact optical properties. In both structures, we observed no significant change in the extinction, absorbance, and scattering spectra, indicating that the interior features are still relatively large to contribute to a significant loss via λ_e. As the pore walls narrow and become atomistic

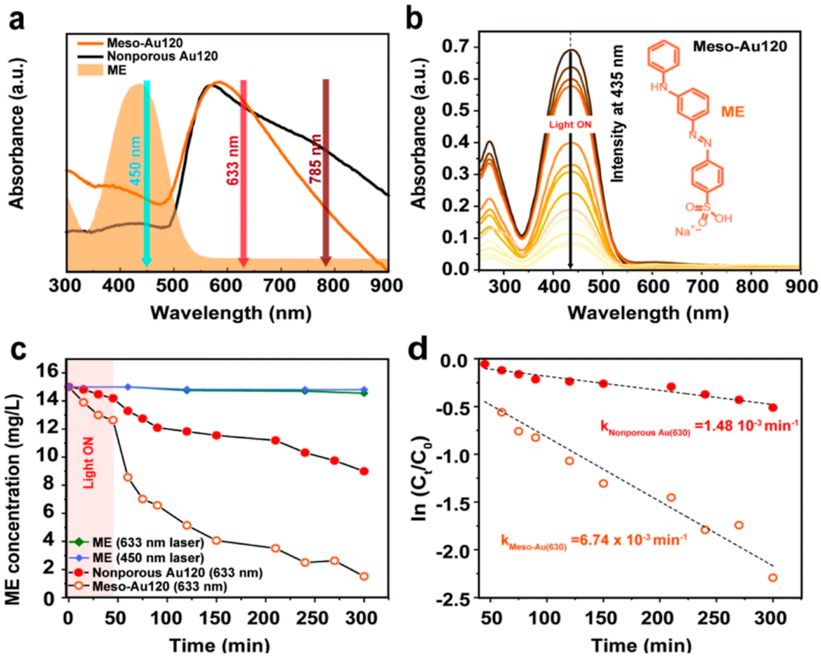

Figure 7. Photocatalytic performance of mesoporous Au NPs vs nonporous Au NPs. (a) Optical spectra of ME, meso-Au120, nonporousAu120, and marked laser wavelengths used in this study, (b) UV spectra for photodegradation of ME using meso-Au120, (c) kinetic measurements of ME plasmon-driven degradation using meso-Au120 and nonporous Au120 with 633 and 450 nm laser and corresponding photodegradation kinetic curves using first-order reaction fitting (d).

junctions, nonlocal effects such as spatial dispersion emerge and require more sophisticated models to quantify absolute loss mechanisms.[83]

Plasmon-Enhanced Photocatalysis with Mesoporous Au Nanoparticles. In the context of photocatalysis, symmetry breaking with mesopores is advantageous over other methods using NPs with dielectric[80] and metal[81] substrates in addition to core−shell NPs[84] because mesoporous metals expose more of the metal surface to the environment. This can lead to a synergistic effect where E-fields from hybridized modes are colocalized to regions with numerous atomic step edges and kinks where catalytic active sites in metals are most dense. Porosity is also important in organic catalytic transformations because it maximizes the number of interaction events between the reactant, metal surface, and plasmon-driven electric field (and any resulting heat). To examine the effect of the plasmon on an organic reaction, we used the plasmon-driven degradation of metanil yellow (ME) as a model reaction. ME is an azo-dye that is an environmental pollutant[85] and a known carcinogen[86] that absorbs strongly at blue wavelengths. We examined the photocatalytic performance of meso-Au120 NP because it has the largest surface area as estimated with ECSA and supports hybridized plasmon modes. We used nonporous 120 nm diameter Au NPs (i.e., "nonporous Au120") to compare performance in the plasmon-enhanced degradation of aqueous ME because both particles have similar plasmon resonances in a similar range (550−650 nm) and were found to have a large electrochemically active surface area in EOR. An equal amount of meso-Au120 and nonporous Au120 were mixed with 15 mg/L ME and illuminated with diodes at various excitation wavelengths (λ_{ex} = 450, 633, and 785 nm). The kinetic rate of degradation was tracked using the ME absorbance peak at 435 nm (Figure 7a,b). Control experiments illuminating neat ME in water using 450 and 633 nm light showed negligible photodissociation (Figure 7c,d).

According to the kinetic measurements (Figure 7b,c), mixing of meso-Au120 with ME solution led to the adsorption of ME inside meso-Au120 pores within the first 45 min (Figure 7b). Further illumination with 633 nm laser light led to a significant decrease in ME concentration with almost quantitative degradation within 300 min. We also calculated the kinetic rate constants using the first-order kinetic equation: $\ln(C_t/C_0) = -kt$. The $k_{\text{meso-Au}}$ was found to be 6.74×10^{-3} min^{-1} for λ_{ex} = 633 nm. In the case of nonporous Au120 NP, no adsorption was observed after mixing; photocatalytic ME degradation at λ_{ex} = 633 nm proceeded with $k_{\text{nonporous Au}} = 1.48 \times 10^{-3}$ min^{-1}. The increase in plasmon-driven degradation rate by 4.5 times indicates the impact of the porous gold structure. We examined ME degradation on meso-Au120 using λ_{ex} = 450 and 785 nm to observe the effect of irradiation off-resonance in the regions where Au permittivity has a high and low imaginary component, respectively (Figure S27). In both cases, ME photodegradation was ∼10× less efficient than λ_{ex} = 633 which overlaps primarily with the hybridized D plasmon mode. These results show that NPs with mesoporous structures promote plasmon-driven reactions, enabling researchers to use more gentle reaction conditions (i.e., lower temperature, pressure, reaction time, and catalyst amount) compared to nonporous NPs. Tuning porosity has a dual effect on both the number and density of active sites of the metal and the wavelength and bandwidth of the plasmon resonances.

■ CONCLUSIONS

We have developed a simple wet chemical strategy to synthesize mesoporous Au NPs with large pores via the chemical reduction in the presence of the diblock copolymer PS-*b*-PEO BCMs and L-Cys thiol ligand. The role of L-Cys is to form a dense Au(I)−thiolate metallogel matrix around the BCMs, effectively trapping BCMs so that the metal can be reduced around them. Delegating metallogel formation to L-

Cys instead of a functional group covalently bound to the micelle allows us to use commercially available BCMs as opposed to bespoke custom-synthesized molecules. The combination of L-Cys and AA enables more control over the reduction reaction because the reaction is more gentle. Surprisingly, we observed the presence of Au nanoclusters which are even less mobile and indicate that the NPs form via a complex pathway from Au^{3+} to Au(I)−thiolates to clusters to NPs. The diameters and pore sizes of the as-prepared mesoporous Au NPs were highly uniform and had a narrow size distribution. Control over particle size is achieved by changing the KOH concentration, while tailoring the different pore sizes of the Au NPs could be obtained by changing the molecular weight of the BCMs. We used STEM tomography to make 3D models of different size particles, proving that the pores were dispersed throughout the interior and exterior of the particle. Electrochemistry was used to estimate the reactivity and accessible surface area of the network of pores in the mesoporous Au NPs. In the EOR, surface active sites demonstrated good reactivity and ECSA measurements demonstrate the accessibility of the open porous architecture. Consequently, the mesoporous Au NPs had improved electrocatalytic activity in the EOR compared to nonporous Au NPs with similar sizes. Comparing the tomography models with ECSA is useful because it shows that much of the porous network is accessible to the environment.

The tomography models were input directly into a computational electrodynamics code to describe their plasmon modes and light-focusing properties, which had never been done before for mesoporous metal particles of this size. We used a simple model to show how mesopores in Au NPs induce symmetry breaking, enabling continuous tuning of strongly hybridized D and Q modes via pore size. Increasing pore size subdivides the particles into an interconnected network of nanoscale junctions with local optical conductances that shift the resonance wavelength of the plasmon modes and induce symmetry-breaking of the plasmon modes. Symmetry-breaking has been observed in numerous structures, but these are either solid convex structures with minimal surface area or are NP clusters held together with weak van der Waals forces or chemical bonds. Symmetry-breaking with mesopores is uniquely suited for photocatalysis because it maximizes exposure of the metal surface for catalysis in a rugged free-standing structure that can be suspended in solution. Colocalizing the hybridized plasmon resonances to the porous structure enhances plasmonic reactions. We compared mesoporous Au NPs to nonporous Au NPs using the plasmon-driven degradation of ME. Mesoporous NPs had a photocatalytic degradation rate ~4.5-times faster than the nonporous Au NPs and achieved almost quantitative degradation of ME. Mesoporous NPs can be synthesized in numerous plasmonic metals, alloys, and metal borides. Designing plasmonic structures that colocalize electric fields with active sites and maximize interaction with the plasmon-driven electric field should enable light-driven organic transformations using more gentle reaction conditions.

■ EXPERIMENTAL DETAILS

Materials. Polystyrene-*b*-poly(ethylene oxide) (PS-*b*-PEO) diblock copolymers with 18,000 (PS) and 7500 (PEO) molecular weight subunits were acquired from the Polymer Source. THF, tetrachloroauric acid trihydrate ($HAuCl_4 \cdot 3H_2O$), potassium hydroxide (KOH), sodium hydroxide (NaOH), polyvinylpyrrolidone (PVP), trisodium citrate (Na_3Ctr), L-ascorbic acid (AA), and *trans*-2-[3-(4-*tert*-butylphenyl)-2-methyl-2-propenylidene]malononitrile (DCTB, ≥99%), dichloromethane, glutathione, *p*-mercaptobenzoic, and hydrazine were purchased from the Sigma-Aldrich. Ethanol, L-Cys, and ME (Acid Yellow 36) were purchased from the Merck and Tokyo chemical industry. All chemicals were used without further purification. Deionized water was obtained with a Milli-Q water purification system (18.2 MΩ·cm) and used to prepare aqueous solutions.

Preparation of Mesoporous Au Nanoparticles. BCMs were used as pore-directing agents to assemble the mesoporous Au NPs in the presence of a chemical reducing agent. In a typical synthesis, 1.25 mg of polystyrene-*b*-poly(ethylene oxide) ($PS_{18,000}$-*b*-PEO_{7500}) was completely dissolved in 0.25 mL of THF at 40 °C. Then 125 μL of ethanol, 57 μL of 750 mM KOH, and 127 μL of aqueous 10 mM L-Cys were added to the abovementioned solution in sequence and mixed for 20 min in an ice bath under gentle stirring. Then a cold solution of aqueous 80 mM $HAuCl_4$ (188 μL) followed by 100 mM AA (250 μL) was added to the abovementioned solution and stirred for 2 min. In this timeframe, the color of the solution changed from dark transparent yellow to colorless, then red-blue as the final product was generated. The reaction mixture was stirred for another 1 h in the ice bath. The samples were collected by centrifugation at 14,000 rpm for 15 min and then washed using THF/ethanol (1:1) and centrifuged again. This process was repeated 8-times to remove the polymer micelle templates. The impact of other thiol ligands such as glutathione and *p*-mercaptobenzoic were examined and compared with L-Cys.

Preparation of Nonporous Quasi-Spherical Au Nanoparticles as Experimental Controls in Electrocatalysis. Au NPs with an average diameter of 30 nm were initially synthesized to serve as seeds to generate large NPs. An aqueous solution (2 mL) containing PVP (280 mM) and $HAuCl_4$ (5 mM) was added to a flask under gentle stirring. Then 0.5 mL of 30 mM AA was quickly added to the mixture. The solution changed from colorless to red, indicating the formation of small Au NPs ("seed solution"). Next, 227 μL of 80 mM $HAuCl_4$, 39.6 μL of water, and 176 μL 40 mM Na_3Ctr were added to a 2 mL vial and gently mixed, then 150 μL of the seed solution was added, and the whole solution was mixed at room temperature for 1 h. Finally, the product was washed with water and followed by centrifugation at 14,000 rpm for 5 min.

Characterization. The morphology and interior structure of the mesoporous Au NPs was initially checked with a field-emission scanning electron microscope (SEM, JEOL JSM-7100F; 15 kV) and a transmission electron microscope (TEM, Hitachi HF5000; 200 kV). Raman spectra were recorded on a laser-scanning Raman microscope (Renishaw) using an excitation wavelength of $\lambda = 785$ nm. UV−vis absorption spectra were collected on a Cary 4000 UV−Vis spectrometer. MALDI-TOF mass spectrometry measurements were carried out using a JEOL Spiral TOF with the matrix of DCTB in dichloromethane. The ratio of matrix to analyte was 1:100 and mixed in a microcentrifuge tube; 1 μL of this solution was dried on the sample plate in air. An X-ray diffractometer was used to examine the crystallinity of the samples (XRD; Rigaku Smartlab; Cu Kα 40 kV, 40 mA at 2° min^{-1}). The spacing of the pores was measured by using SAXS (Rigaku NANO-Viewer; 40 kV, 30 mA at 700 mm). The 3D structure of one of the particles was examined using scanning TEM tomography using a high-angle annular dark-field detector (STEM-HAADF-tomography, Thermo Scientific TALOS F200X). The tomography sections were acquired using a 400 nm field of view with a dwell time of 2 μs and tilted from −69 to +69° and acquired at 3° increments. The images were aligned and converted into 3D stacks using a software package called Inspect3D. Then the samples were converted into a 3D image using Fiji (ImageJ) bundle and then transformed into an STL file. The resulting STL file was then imported into a 3D EM simulator (Lumerical-Ansys). The optical properties of Au were simulated using optical constants from McPeak.[77] The background refractive index of the simulation was set to $n = 1.333$ to mimic water.

Electrochemical Characterization. CV and CA measurements were carried out on a CHI 760E electrochemical analyzer (CHI Instrument, USA). All electrochemical measurements were performed with a three-electrode configuration: a Pt wire counter electrode, a standard calomel electrode (SCE) reference electrode, and a glassy carbon working electrode coated with the Au catalyst. Unless stated otherwise, all potentials are reported versus SCE. All catalysts were dispersed via ultrasonication (1 mg mL^{-1}), and then, a tiny amount (2 μL) of this suspension was drop-cast onto the glassy carbon electrode surface and dried in air for 12 h. The ECSA of the sample was measured using CV in the 0.5 M H_2SO_4 at a scan rate of 50 mV s^{-1}. The charge passed during the reduction of oxide monolayer on Au was recorded and integrated from the current during the reduction of gold oxide. By following the equation of $Q_o = 2eNA\Gamma_o A$, where Q_o is the charge passed associated with the reduction of oxide monolayer and on the basic assumption that the charge associated with the reduction of oxide species on the smooth Au surface is equivalent to 400 μC cm^{-2}, the ECSA of the sample is $A = Q_o/400$ μC cm^{-2} area.[87] Specific surface area was obtained by dividing the ECSA by the sample mass. Before all analytical electrochemical measurements, the electrode was activated via CV in 1 M NaOH over a potential window of −1 to 0.6 V until the curves became stable and exhibited the typical behavior of a clean Au electrode. All electrochemistry experiments were carried out at room temperature.

Degradation Experiments. Degradation experiments were studied with a concentration of ME of 15 mg/L. The plasmonic degradation was performed using 2 mL of ME solution with meso-Au120 or nonporous Au120 (17 mg/L) in a quartz cuvette, and the system was mixed using magnetic stirring (200 rpm) for 45 min and subjected to 633 nm (laser, Thorlabs, PL450B), 450 nm (laser, Thorlabs, HL63163DG) or 785 nm (LED, Thorlabs, P M780LP1) irradiation (60 mW). The probes (150 μL) were taken after a definite time, centrifugated to remove Au NPs, and 100 μL ME was analyzed by UV−vis to quantify absorbance at 435 nm.

For the quantitative evaluation of the degradation efficacy, a pseudo-first kinetic model has been suggested. Therefore, the obtained kinetic data were fitted according to the equation

$$\ln(C_t/C_0) = -kt$$

where C_t (mg/L)—the concentration of the solution at time t; C_0 (mg/L)—the initial concentration of ME, t (min)—the time of illumination, and k—the first-order rate constant.

■ ASSOCIATED CONTENT

Supporting Information

The Supporting Information is available free of charge at https://pubs.acs.org/doi/10.1021/acs.chemmater.2c01125.

> SEM, TEM, and SAXS data describing particle size and pore wall size estimates; UV−vis and Raman data examining particle growth; electrochemistry measurements examining the surface area and reactivity of the various mesoporous Au NPs and comparison to the performance of other materials in the literature; and optical simulations of solid Au spheres and mesoporous Au NPs (PDF)

■ AUTHOR INFORMATION

Corresponding Authors

Joel Henzie − *JST-ERATO Yamauchi Materials Space-Tectonics Project and International Center for Materials Nanoarchitectonics (MANA), National Institute for Materials Science (NIMS), Tsukuba 305-0044 Ibaraki, Japan;* orcid.org/0000-0002-9190-2645; Email: HENZIE.Joeladam@nims.go.jp

Yusuke Yamauchi − *Australian Institute for Bioengineering and Nanotechnology (AIBN), The University of Queensland, Brisbane 4072 Queensland, Australia; JST-ERATO Yamauchi Materials Space-Tectonics Project and International Center for Materials Nanoarchitectonics (MANA), National Institute for Materials Science (NIMS), Tsukuba 305-0044 Ibaraki, Japan;* orcid.org/0000-0001-7854-927X; Email: y.yamauchi@uq.edu.au

Authors

Asep Sugih Nugraha − *Australian Institute for Bioengineering and Nanotechnology (AIBN), The University of Queensland, Brisbane 4072 Queensland, Australia*

Olga Guselnikova − *JST-ERATO Yamauchi Materials Space-Tectonics Project and International Center for Materials Nanoarchitectonics (MANA), National Institute for Materials Science (NIMS), Tsukuba 305-0044 Ibaraki, Japan;* orcid.org/0000-0002-2594-9605

Jongbeom Na − *Materials Architecturing Research Center, Korea Institute of Science and Technology, Seoul 02792, Republic of Korea; Australian Institute for Bioengineering and Nanotechnology (AIBN), The University of Queensland, Brisbane 4072 Queensland, Australia;* orcid.org/0000-0002-3890-7877

Md Shahriar A. Hossain − *Australian Institute for Bioengineering and Nanotechnology (AIBN), The University of Queensland, Brisbane 4072 Queensland, Australia; School of Mechanical & Mining Engineering, The University of Queensland, Brisbane 4072 Queensland, Australia*

Ömer Dag − *Department of Chemistry and UNAM-National Nanotechnology Research Center, Bilkent University, Ankara 06800, Turkey;* orcid.org/0000-0002-1129-3246

Alan E. Rowan − *Australian Institute for Bioengineering and Nanotechnology (AIBN), The University of Queensland, Brisbane 4072 Queensland, Australia*

Complete contact information is available at: https://pubs.acs.org/10.1021/acs.chemmater.2c01125

Notes

The authors declare no competing financial interest.

■ ACKNOWLEDGMENTS

This work was funded by the Japan Society for the Promotion of Science (JSPS) Grants-in-Aid for Scientific Research Kakenhi Program (20K05453) and the JST-ERATO Materials Space-Tectonics Project (JPMJER2003). The researchers also acknowledge the LaSensA project under the M-ERA.NET scheme funded by the Research Council of Lithuania (LMTLT, agreement no. S-M-ERA.NET-21-2), Saxon State Ministry for Science, Culture and Tourism (Germany), and the National Science Centre (Poland) and the Basic Science Research Program through the National Research Foundation of Korea (NRF) funded by the Ministry of Education (2020R1A6A3A03039037). O.G. thanks the JSPS Postdoctoral Fellowship program. This work was partially performed at the University of Queensland (UQ) node of the Australian National Fabrication Facility (ANFF-Q), a company established under the National Collaborative Research Infrastructure Strategy to provide nano- and micro-fabrication facilities for Australian researchers. The authors thank Makoto Oishi at the NIMS Electron Microscope Analysis Station in the High-Resolution Group for technical assistance with the STEM tomography measurements. The authors also acknowledge the facilities and scientific and technical assistance of the

UQ Australian Microscopy & Microanalysis Research Facility and the University of Queensland.

REFERENCES

(1) Kresge, C. T.; Leonowicz, M. E.; Roth, W. J.; Vartuli, J. C.; Beck, J. S. Ordered mesoporous molecular sieves synthesized by a liquid-crystal template mechanism. *Nature* **1992**, *359*, 710−712.

(2) Yanagisawa, T.; Shimizu, T.; Kuroda, K.; Kato, C. The preparation of alkyltrimethylammonium-kanemite complexes and their conversion to microporous materials. *Bull. Chem. Soc. Jpn.* **1990**, *63*, 988−992.

(3) Yang, P.; Zhao, D.; Margolese, D. I.; Chmelka, B. F.; Stucky, G. D. Block copolymer templating syntheses of mesoporous metal oxides with large ordering lengths and semicrystalline framework. *Chem. Mater.* **1999**, *11*, 2813−2826.

(4) Yang, P.; Zhao, D.; Margolese, D. I.; Chmelka, B. F.; Stucky, G. D. Generalized syntheses of large-pore mesoporous metal oxides with semicrystalline frameworks. *Nature* **1998**, *396*, 152−155.

(5) Lee, J.; Yoon, S.; Hyeon, T.; Oh, S. M.; Kim, K. B. Synthesis of a new mesoporous carbon and its application to electrochemical double-layer capacitors. *Chem. Commun.* **1999**, 2177−2178.

(6) Liang, C.; Dai, S. Synthesis of mesoporous carbon materials via enhanced hydrogen-bonding interaction. *J. Am. Chem. Soc.* **2006**, *128*, 5316−5317.

(7) Attard, G. S.; Bartlett, P. N.; Coleman, N. R. B.; Elliott, J. M.; Owen, J. R.; Wang, J. H. Mesoporous platinum films from lyotropic liquid crystalline phases. *Science* **1997**, *278*, 838−840.

(8) Malgras, V.; Ataee-Esfahani, H.; Wang, H.; Jiang, B.; Li, C.; Wu, K. C.-W.; Kim, J. H.; Yamauchi, Y. Nanoarchitectures for mesoporous metals. *Adv. Mater.* **2016**, *28*, 993−1010.

(9) Arruebo, M. Drug delivery from structured porous inorganic materials. *Wiley Interdiscip. Rev.: Nanomed. Nanobiotechnol.* **2012**, *4*, 16−30.

(10) Nugraha, A. S.; Na, J. M. S. A.; Hossain, J.; Lin, Y. V.; Kaneti, M.; Iqbal, B.; Jiang, Y.; Bando, T.; Asahi, Y.; Yamauchi, Y. Block copolymer-templated electrodeposition of mesoporous Au-Ni alloy films with tunable composition. *Appl. Mater. Today* **2020**, *18*, 100526.

(11) Ling, P.; Zhang, Q.; Cao, T.; Gao, F. Versatile Three-Dimensional Porous Cu@Cu_2O Aerogel Networks as Electrocatalysts and Mimicking Peroxidases. *Angew. Chem., Int. Ed.* **2018**, *57*, 6819−6824.

(12) Bernsmeier, D.; Polte, J.; Ortel, E.; Krahl, T.; Kemnitz, E.; Kraehnert, R. Antireflective coatings with adjustable refractive index and porosity synthesized by Micelle-templated deposition of MgF_2 sol particles. *ACS Appl. Mater. Interfaces* **2014**, *6*, 19559−19565.

(13) Chen, Y.; Yu, Z.; Zheng, K.; Ren, Y.; Wang, M.; Wu, Q.; Zhou, F.; Liu, C.; Liu, L.; Song, J.; Qu, J. Degradable mesoporous semimetal antimony nanospheres for near-infrared II multimodal theranostics. *Nat. Commun.* **2022**, *13*, 539.

(14) Yu, P.; Liang, Y.; Dong, H.; Hu, H.; Liu, S.; Peng, L.; Zheng, M.; Xiao, Y.; Liu, Y. Rational synthesis of highly porous carbon from waste bagasse for advanced supercapacitor application. *ACS Sustainable Chem. Eng.* **2018**, *6*, 15325−15332.

(15) Lee, J.-S.; Kim, S.-I.; Yoon, J.-C.; Jang, J.-H. Chemical vapor deposition of mesoporous graphene nanoballs for supercapacitor. *ACS Nano* **2013**, *7*, 6047−6055.

(16) Jiang, B.; Guo, Y.; Kim, J.; Whitten, A. E.; Wood, K.; Kani, K.; Rowan, A. E.; Henzie, J.; Yamauchi, Y. Mesoporous Metallic Iridium Nanosheets. *J. Am. Chem. Soc.* **2018**, *140*, 12434−12441.

(17) Iqbal, M.; Kim, Y.; Saputro, A. G.; Shukri, G.; Yuliarto, B.; Lim, H.; Nara, H.; Alothman, A. A.; Na, J.; Bando, Y.; Yamauchi, Y. Tunable concave surface features of mesoporous palladium nanocrystals prepared from supramolecular micellar templates. *ACS Appl. Mater. Interfaces* **2020**, *12*, 51357−51365.

(18) Zhang, Q.; Wang, H. Facet-dependent catalytic activities of Au nanoparticles enclosed by high-index facets. *ACS Catal.* **2014**, *4*, 4027−4033.

(19) Prodan, E.; Radloff, C.; Halas, N. J.; Nordlander, P. A Hybridization Model for the Plasmon Response of Complex Nanostructures. *Science* **2003**, *302*, 419−422.

(20) Fan, J. A.; Wu, C.; Bao, K.; Bao, J.; Bardhan, R.; Halas, N. J.; Manoharan, V. N.; Nordlander, P.; Shvets, G.; Capasso, F. Self-assembled plasmonic nanoparticle clusters. *Science* **2010**, *328*, 1135−1138.

(21) Iqbal, M.; Bando, Y.; Sun, A. G.; Wu, G.; Rowan, B.; Na, H.; Guan, H.; Yamauchi, A. A.; Na, J.; Bando, Y.; Yamauchi, Y. In Search of Excellence: Convex versus Concave Noble Metal Nanostructures for Electrocatalytic Applications. *Adv. Mater.* **2021**, *33*, 2004554.

(22) Tao, A. R.; Habas, S.; Yang, P. Shape control of colloidal metal nanocrystals. *Small* **2008**, *4*, 310−325.

(23) Haruta, M.; Yamada, N.; Kobayashi, T.; Iijima, S. Gold catalysts prepared by coprecipitation for low-temperature oxidation of hydrogen and of carbon monoxide. *J. Catal.* **1989**, *115*, 301−309.

(24) Cao, X.; Li, C.; Peng, D.; Lu, Y.; Huang, K.; Wu, J.; Zhao, C.; Huang, Y. Highly strained au nanoparticles for improved electrocatalysis of ethanol oxidation reaction. *J. Phys. Chem. Lett.* **2020**, *11*, 3005−3013.

(25) Xu, X.; Jia, J.; Yang, X.; Dong, S. A templateless, surfactantless, simple electrochemical route to a dendritic gold nanostructure and its application to oxygen reduction. *Langmuir* **2010**, *26*, 7627−7631.

(26) Liu, K.; Bai, Y.; Zhang, L.; Yang, Z.; Fan, Q.; Zheng, H.; Yin, Y.; Gao, C. Porous Au-Ag nanospheres with high-density and highly accessible hotspots for SERS analysis. *Nano Lett.* **2016**, *16*, 3675−−3681.

(27) Wei, X.; Fan, Q.; Liu, H.; Bai, Y.; Zhang, L.; Zheng, H.; Yin, Y.; Gao, C. Holey Au-Ag alloy nanoplates with built-in hotspots for surface-enhanced Raman scattering. *Nanoscale* **2016**, *8*, 15689−15695.

(28) Pedireddy, S.; Lee, H. K.; Tjiu, W. W.; Phang, I. Y.; Tan, H. R.; Chua, S. Q.; Troadec, C.; Ling, X. Y. One-step synthesis of zero-dimensional hollow nanoporous gold nanoparticles with enhanced methanol electrooxidation performance. *Nat. Commun.* **2014**, *5*, 4947.

(29) Hu, J.; Jiang, R.; Zhang, H.; Guo, Y.; Wang, J.; Wang, J. Colloidal porous gold nanoparticles. *Nanoscale* **2018**, *10*, 18473−18481.

(30) Tranchant, M.; Serrà, A.; Gunderson, C.; Bertero, E.; García-Amorós, J.; Gómez, E.; Michler, J.; Philippe, L. Efficient and green electrochemical synthesis of 4-aminophenol using porous Au micropillars. *Appl. Catal., A* **2020**, *602*, 117698.

(31) Sattayasamitsathit, S.; Gu, Y.; Kaufmann, K.; Minteer, S.; Polsky, R.; Wang, J. Tunable hierarchical macro/mesoporous gold microwires fabricated by dual-templating and dealloying processes. *Nanoscale* **2013**, *5*, 7849−7854.

(32) Yu, H.; Qiu, X.; Nunes, S. P.; Peinemann, K.-V. Self-assembled isoporous block copolymer membranes with tuned pore sizes. *Angew. Chem., Int. Ed.* **2014**, *53*, 10072−10076.

(33) Lim, H.; Kani, K.; Henzie, J.; Nagaura, T.; Nugraha, A. S.; Iqbal, M.; Ok, Y. S.; Hossain, M. S. A.; Bando, Y.; Wu, K. C. W.; Kim, H.-J.; Rowan, A. E.; Na, J.; Yamauchi, Y. A universal approach for the synthesis of mesoporous gold, palladium and platinum films for applications in electrocatalysis. *Nat. Protoc.* **2020**, *15*, 2980−3008.

(34) Jiang, B.; Li, C.; Dag, Ö.; Abe, H.; Takei, T.; Imai, T.; Hossain, M. S. A.; Islam, M. T.; Wood, K.; Henzie, J.; Yamauchi, Y. Mesoporous metallic rhodium nanoparticles. *Nat. Commun.* **2017**, *8*, 15581.

(35) Iqbal, M.; Kim, Y.; Li, C.; Jiang, B.; Takei, T.; Lin, J.; Yuliarto, B.; Bando, Y.; Henzie, J.; Yamauchi, Y. Tailored design of mesoporous PdCu nanospheres with different compositions using polymeric micelles. *ACS Appl. Mater. Interfaces* **2019**, *11*, 36544−36552.

(36) Jiang, B.; Song, H.; Kang, Y.; Wang, S.; Wang, Q.; Zhou, X.; Kani, K.; Guo, Y.; Ye, J.; Li, H.; Sakka, Y.; Henzie, J.; Yusuke, Y. A mesoporous non-precious metal boride system: Synthesis of mesoporous cobalt boride by strictly controlled chemical reduction. *Chem. Sci.* **2020**, *11*, 791−796.

(37) Zou, Y.; Zhou, X.; Zhu, Y.; Cheng, X.; Zhao, D.; Deng, Y. sp^2-Hybridized Carbon-Containing Block Copolymer Templated Syn-

thesis of Mesoporous Semiconducting Metal Oxides with Excellent Gas Sensing Property. *Acc. Chem. Res.* **2019**, *52*, 714−725.

(38) Zou, Y.; Zhou, X.; Ma, J.; Yang, X.; Deng, Y. Recent advances in amphiphilic block copolymer templated mesoporous metal-based materials: assembly engineering and applications. *Chem. Soc. Rev.* **2020**, *49*, 1173−1208.

(39) Jiang, B.; Li, C.; Tang, J.; Takei, T.; Kim, J. H.; Ide, Y.; Henzie, J.; Tominaka, S.; Yamauchi, Y. Tunable-sized polymeric micelles and their assembly for the preparation of large mesoporous platinum nanoparticles. *Angew. Chem., Int. Ed.* **2016**, *55*, 10037−10041.

(40) Lv, H.; Xu, D.; Henzie, J.; Feng, J.; Lopes, A.; Yamauchi, Y.; Liu, B. Mesoporous gold nanospheres: Via thiolate-Au(I) intermediates. *Chem. Sci.* **2019**, *10*, 6423−6430.

(41) Schmidbaur, H.; Schier, A. Aurophilic interactions as a subject of current research: An up-date. *Chem. Soc. Rev.* **2012**, *41*, 370−412.

(42) Templeton, A. C.; Wuelfing, W. P.; Murray, R. W. Monolayer-protected cluster molecules. *Acc. Chem. Res.* **2000**, *33*, 27−36.

(43) Li, Y.; Higaki, T.; Du, X.; Jin, R. Chirality and surface bonding correlation in atomically precise metal nanoclusters. *Adv. Mater.* **2020**, *32*, 1905488.

(44) Jiang, W.; Qu, Z.-B.; Kumar, P.; Vecchio, D.; Wang, Y.; Ma, Y.; Bahng, J. H.; Bernardino, K.; Gomes, W. R.; Colombari, F. M.; Lozada-Blanco, A.; Veksler, M.; Marino, E.; Simon, A.; Murray, C.; Muniz, S. R.; de Moura, A. F.; Kotov, N. A. Emergence of complexity in hierarchically organized chiral particles. *Science* **2020**, *368*, 642−648.

(45) Li, C.; Iqbal, M.; Jiang, B.; Wang, Z.; Kim, J.; Nanjundan, A. K.; Whitten, A. E.; Wood, K.; Yamauchi, Y. Pore-tuning to boost the electrocatalytic activity of polymeric micelle-templated mesoporous Pd nanoparticles. *Chem. Sci.* **2019**, *10*, 4054−4061.

(46) Ma, J.; Li, Y.; Li, J.; Yang, X.; Ren, Y.; Alghamdi, A. A.; Song, G.; Yuan, K.; Deng, Y. Rationally Designed Dual-Mesoporous Transition Metal Oxides/Noble Metal Nanocomposites for Fabrication of Gas Sensors in Real-Time Detection of 3-Hydroxy-2-Butanone Biomarker. *Adv. Funct. Mater.* **2022**, *32*, 2107439.

(47) Nasaruddin, R. R.; Chen, T.; Yan, N.; Xie, J. Roles of thiolate ligands in the synthesis, properties and catalytic application of gold nanoclusters. *Coord. Chem. Rev.* **2018**, *368*, 60−79.

(48) Shichibu, Y.; Negishi, Y.; Tsunoyama, H.; Kanehara, M.; Teranishi, T.; Tsukuda, T. Extremely high stability of glutathionate-protected Au_{25} clusters against core etching. *Small* **2007**, *3*, 835−839.

(49) Bertorelle, F.; Russier-Antoine, I.; Comby-Zerbino, C.; Chirot, F.; Dugourd, P.; Brevet, P.-F.; Antoine, R. Isomeric effect of mercaptobenzoic acids on the synthesis, stability, and optical properties of $Au_{25}(MBA)_{18}$ nanoclusters. *ACS Omega* **2018**, *3*, 15635−15642.

(50) Alvarez, M. M.; Khoury, J. T.; Schaaff, T. G.; Shafigullin, M.; Vezmar, I.; Whetten, R. L. Critical sizes in the growth of au clusters. *Chem. Phys. Lett.* **1997**, *266*, 91−98.

(51) Varnholt, B.; Oulevey, P.; Luber, S.; Kumara, C.; Dass, A.; Bürgi, T. Structural Information on the Au-S Interface of Thiolate-Protected Gold Clusters: A Raman Spectroscopy Study. *J. Phys. Chem. C* **2014**, *118*, 9604−9611.

(52) Söptei, B.; Naszályi Nagy, L.; Baranyai, P.; Szabó, I.; Mező, G.; Hudecz, F.; Bóta, A. On the selection and design of proteins and peptide derivatives for the production of photoluminescent, red-emitting gold quantum clusters. *Gold Bull.* **2013**, *46*, 195−203.

(53) Xie, J.; Zheng, Y.; Ying, J. Y. Protein-directed synthesis of highly fluorescent gold nanoclusters. *J. Am. Chem. Soc.* **2009**, *131*, 888−889.

(54) Borghei, Y.-S.; Hosseini, M.; Khoobi, M.; Ganjali, M. R. Novel fluorometric assay for detection of cysteine as a reducing agent and template in formation of copper nanoclusters. *J. Fluoresc.* **2017**, *27*, 529−536.

(55) Yang, X.; Feng, Y.; Zhu, S.; Luo, Y.; Zhuo, Y.; Dou, Y. One-step synthesis and applications of fluorescent Cu nanoclusters stabilized by l-cysteine in aqueous solution. *Anal. Chim. Acta* **2014**, *847*, 49−54.

(56) Yuan, X.; Zhang, B.; Luo, Z.; Yao, Q.; Leong, D. T.; Yan, N.; Xie, J. Balancing the rate of cluster growth and etching for gram-scale synthesis of thiolate-protected Au_{25} nanoclusters with atomic precision. *Angew. Chem., Int. Ed.* **2014**, *53*, 4623−4627.

(57) Baghdasaryan, A.; Grillo, R.; Roy Bhattacharya, S.; Sharma, M.; Reginato, E.; Theraulaz, H.; Dolamic, I.; Dadras, M.; Rudaz, S.; Varesio, E.; Burgi, T. Facile synthesis, size-separation, characterization, and antimicrobial properties of thiolated copper clusters. *ACS Appl. Nano Mater.* **2018**, *1*, 4258−4267.

(58) Kumar, N.; Upadhyay, L. S. B. Facile and green synthesis of highly stable L-cysteine functionalized copper nanoparticles. *Appl. Surf. Sci.* **2016**, *385*, 225−233.

(59) Cappellari, P. S.; Buceta, D.; Morales, G. M.; Barbero, C. A.; Sergio Moreno, M.; Giovanetti, L. J.; Ramallo-López, J. M.; Requejo, F. G.; Craievich, A. F.; Planes, G. A. Synthesis of ultra-small cysteine-capped gold nanoparticles by pH switching of the Au(I)-cysteine polymer. *J. Colloid Interface Sci.* **2015**, *441*, 17−24.

(60) Guo, M.; He, J.; Li, Y.; Ma, S.; Sun, X. One-step synthesis of hollow porous gold nanoparticles with tunable particle size for the reduction of 4-nitrophenol. *J. Hazard. Mater.* **2016**, *310*, 89−97.

(61) Qin, Y.; Ji, X.; Jing, J.; Liu, H.; Wu, H.; Yang, W. Size control over spherical silver nanoparticles by ascorbic acid reduction. *Colloids Surf., A* **2010**, *372*, 172−276.

(62) Jana, N. R.; Gearheart, L.; Murphy, C. J. Seed-mediated growth approach for shape-controlled synthesis of spheroidal and rod-like gold nanoparticles using a surfactant template. *Adv. Mater.* **2001**, *13*, 1389−1393.

(63) Su, D.; Dou, S.; Wang, G. Gold nanocrystals with variable index facets as highly effective cathode catalysts for lithium-oxygen batteries. *NPG Asia Mater.* **2015**, *7*, No. e155.

(64) Liu, Z.-P.; Hu, P. General Rules for Predicting Where a Catalytic Reaction Should Occur on Metal Surfaces: A Density Functional Theory Study of C−H and C−O Bond Breaking/Making on Flat, Stepped, and Kinked Metal Surfaces. *J. Am. Chem. Soc.* **2003**, *125*, 1958−1967.

(65) Weststrate, C. J.; Lundgren, E.; Andersen, J. N.; Rienks, E. D. L.; Gluhoi, A. C.; Bakker, J. W.; Groot, I. M. N.; Nieuwenhuys, B. E. CO adsorption on Au(310) and Au(321): 6-Fold coordinated gold atoms. *Surf. Sci.* **2009**, *603*, 2152−2157.

(66) Zhang, A.; Chen, Y.; Yang, Z.; Huang, Y.; Richter, G.; Schützendübe, P.; Zhong, C.; Wang, Z. Enhanced electrocatalytic activities toward the ethanol oxidation of nanoporous gold prepared via solid-phase reaction. *ACS Appl. Energy Mater.* **2020**, *3*, 336−343.

(67) Bai, J.; Liu, D.; Yang, J.; Chen, Y. Nanocatalysts for electrocatalytic oxidation of ethanol. *ChemSusChem* **2019**, *12*, 2117−2132.

(68) Huang, J.; Liu, Z.; He, C.; Gan, L. M. Synthesis of PtRu nanoparticles from the hydrosilylation reaction and application as catalyst for direct methanol fuel cell. *J. Phys. Chem. B* **2005**, *109*, 16644−16649.

(69) Xiong, L.; Sun, Z.; Zhang, X.; Zhao, L.; Huang, P.; Chen, X.; Jin, H.; Sun, H.; Lian, Y.; Deng, Z.; Rümmerli, M. H.; Yin, W.; Zhang, D.; Wang, S.; Peng, Y. Octahedral gold-silver nanoframes with rich crystalline defects for efficient methanol oxidation manifesting a CO-promoting effect. *Nat. Commun.* **2019**, *10*, 3782.

(70) Raj, C. R.; Okajima, T.; Ohsaka, T. Gold nanoparticle arrays for the voltammetric sensing of dopamine. *J. Electroanal. Chem.* **2003**, *543*, 127−133.

(71) Khan, R. K.; Yadavalli, V. K.; Collinson, M. M. Flexible nanoporous gold electrodes for electroanalysis in complex matrices. *ChemElectroChem* **2019**, *6*, 4660−4665.

(72) Henzie, J.; Lee, J.; Lee, M. H.; Hasan, W.; Odom, T. W. Nanofabrication of plasmonic Structures. *Annu. Rev. Phys. Chem.* **2009**, *60*, 147−165.

(73) Ebbesen, T. W.; Lezec, H. J.; Ghaemi, H. F.; Thio, T.; Wolff, P. A. Extraordinary optical transmission through sub-wavelength hole arrays. *Nature* **1998**, *391*, 667−669.

(74) Gao, H.; Henzie, J.; Odom, T. W. Direct evidence for surface plasmon-mediated enhanced light transmission through metallic nanohole arrays. *Nano Lett.* **2006**, *6*, 2104−2108.

https://doi.org/10.1021/acs.chemmater.2c01125
Chem. Mater. 2022, 34, 7256−7270

(75) Sheikholeslami, S. N.; Alaeian, H.; Koh, A. L.; Dionne, J. A. A metafluid exhibiting strong optical magnetism. *Nano Lett.* **2013**, *13*, 4137−4141.

(76) Aubry, A.; Lei, D. Y.; Maier, S. A.; Pendry, J. B. Broadband plasmonic device concentrating the energy at the nanoscale: The crescent-shaped cylinder. *Phys. Rev. B: Condens. Matter Mater. Phys.* **2010**, *82*, 125430.

(77) Bukasov, R.; Ali, T. A.; Nordlander, P.; Shumaker-Parry, J. S. Probing the plasmonic near-field of gold nanocrescent antennas. *ACS Nano* **2010**, *4*, 6639−6650.

(78) Zhang, Q.; Large, N.; Nordlander, P.; Wang, H. Porous Au nanoparticles with tunable plasmon resonances and intense field enhancements for single-particle SERS. *J. Phys. Chem. Lett.* **2014**, *5*, 370−374.

(79) McPeak, K. M.; Jayanti, S. V.; Kress, S. J. P.; Meyer, S.; Iotti, S.; Rossinelli, A.; Norris, D. J. Plasmonic films can easily be better: Rules and recipes. *ACS Photonics* **2015**, *2*, 326−333.

(80) Zhang, S.; Bao, K.; Halas, N. J.; Xu, H.; Nordlander, P. Substrate-induced Fano resonances of a plasmonic nanocube: A route to Increased-Sensitivity Localized Surface Plasmon Resonance Sensors Revealed. *Nano Lett.* **2011**, *11*, 1657−1663.

(81) Knight, M. W.; Wu, Y.; Lassiter, J. B.; Nordlander, P.; Halas, N. J. Substrates Matter: Influence of an Adjacent Dielectric on an Individual Plasmonic Nanoparticle. *Nano Lett.* **2009**, *9*, 2188−2192.

(82) Wen, F.; Zhang, Y.; Gottheim, S.; King, N. S.; Zhang, Yu.; Nordlander, P.; Halas, N. J. Charge transfer plasmons: optical frequency conductances and tunable infrared resonances. *ACS Nano* **2015**, *9*, 6428−6435.

(83) Wiener, A.; Duan, H.; Bosman, M.; Horsfield, A. P.; Pendry, J. B.; Yang, J. K. W.; Maier, S. A.; Fernández-Domínguez, A. I. Electron-energy loss study of nonlocal effects in connected plasmonic nanoprisms. *ACS Nano* **2013**, *7*, 6287−6296.

(84) Wang, H.; Wu, Y.; Lassiter, B.; Nehl, N. J.; Hafner, J. H.; Nordlander, P.; Halas, N. J. Symmetry breaking in individual plasmonic nanoparticles. *Proc. Natl. Acad. Sci. U.S.A.* **2006**, *103*, 10856−10860.

(85) Rawat, D.; Mishra, V.; Sharma, R. S. Detoxification of azo dyes in the context of environmental processes. *Chemosphere* **2016**, *155*, 591−605.

(86) Chung, K.-T. Azo dyes and human health: A review. *J. Environ. Sci. Health, Part C: Environ. Carcinog. Ecotoxicol. Rev.* **2016**, *34*, 233−261.

(87) Trasatti, S.; Petrii, O. A. Real surface area measurements in electrochemistry. *Pure Appl. Chem.* **1991**, *63*, 711−734.